Carbon 254 (2026) 121464

Contents lists available at ScienceDirect

Carbon

journal homepage: www.elsevier.com/locate/carbon

A multifunctional molecular bridge for carbon–silver nanohybrids enabling flexible electronic and biocidal applications

Edoardo Testa [a,1], Simone Raciti [a,1], Davide Gentile [a], Mattia Mondella [a], Francesco Goto [b], Gianlorenzo Bussetti [b], Nina Bono [a], Dario Allevi [a], Alberto Bottari [a], Gabriele Candiani [a], Maurizio Galimberti [a], Vincenzina Barbera [a,*]

[a] Department of Chemistry, Materials and Chemical Engineering "G. Natta", Politecnico di Milano, Via Bassini 6, 20133, Milano, Italy
[b] Department of Physics, Politecnico di Milano, Piazza Leonardo da Vinci 32, Milan, 20133, Italy

ARTICLE INFO

Keywords:
Bifunctional molecular interface
Sustainable functionalization
Graphene-related materials
Pyrrole-functionalization
Conductive inks

ABSTRACT

The integration of antimicrobial activity and electrical conductivity in carbon-based materials requires precise control of surface chemistry and metal-carbon interfaces under scalable conditions. Here, a pyrrole-based dual-function molecular bridge (serinol-pyrrole, SP) is employed as a molecular interface to covalently functionalize sp^2 carbon allotropes and to drive the in situ nucleation of silver nanoparticles via a mild, surfactant-free Tollens-type process. This chemistry enables controlled Ag nanoparticle growth directly on carbon substrates without the use of external reductants.

The functionalization strategy is applicable to different carbon allotropes and is successfully translated to an aqueous high-shear mixing process, demonstrating industrially relevant scalability while preserving structural and electronic properties. The resulting silver-carbon nanohybrids exhibit minimum bactericidal concentrations down to 7 μg/mL, negligible mammalian cytotoxicity, and electrical conductivity suitable for printable formulations. When incorporated into polymeric coatings and conductive inks, the materials achieve >99.9% bacterial reduction and stable piezoresistive behavior at significantly reduced silver loadings.

These results demonstrate how interface-engineered carbon surfaces can enable multifunctional performance through scalable chemistry, offering a general route to silver-carbon nanohybrids with controlled structure and properties.

1. Introduction

sp^2-carbon-based materials, including graphene-related materials, carbon nanotubes, and carbon black, generally referred as Carbon Allotropes (CA), are widely employed in functional coatings, electronic devices, and composite systems owing to their high surface area, electrical conductivity, mechanical robustness, and chemical stability [1–3].

The ability to tailor the surface chemistry of sp^2 carbon allotropes while maintaining their intrinsic structural and electronic properties remains a central challenge in carbon science [1,4]. In particular, scalable and controllable functionalization strategies that enable interfacial interactions with inorganic phases are required to expand the functional scope of carbon materials without compromising processability or performance.

Silver nanoparticles (AgNPs) are widely investigated as functional additives due to their high surface reactivity and well-established antimicrobial activity [5,6]. However, their practical implementation is often limited by colloidal instability, aggregation, and poor control over surface distribution, which reduce interfacial efficiency and increase the required metal loading [6,7].

Among metal-carbon hybrid systems, silver-decorated carbon materials are of particular interest due to the combined electrical functionality of carbon substrates and the well-established antimicrobial activity of silver nanoparticles [5,8–10]. Anchoring AgNPs onto graphene-related materials and other sp^2 carbon allotropes represents an effective strategy to stabilize metal nanoparticles, exploit the high surface area and mechanical robustness of carbon substrates, and promote strong metal-carbon interfacial interactions [11–14]. However,

* Corresponding author.
E-mail address: vincenzina.barbera@polimi.it (V. Barbera).
[1] These authors contributed equally to this work.

https://doi.org/10.1016/j.carbon.2026.121464
Received 3 February 2026; Received in revised form 7 March 2026; Accepted 12 March 2026
Available online 20 March 2026

conventional approaches to Ag-carbon hybridization often rely on strong chemical reductants, surfactants, or energy-intensive conditions, which can lead to poor control over nanoparticle nucleation, aggregation, and weak interfacial interactions with the carbon surface [13,15]. These limitations hinder scalability and restrict the efficient use of silver, particularly when low metal loadings and uniform dispersion are required for advanced functional applications. For example, several studies rely on the in situ reduction of silver nitrate ($AgNO_3$) in the presence of graphene oxide (GO) or reduced graphene oxide (rGO). It should be noted that these procedures often result in carbon allotropes characterized by significant lattice defects and structural damage, resulting from the harsh oxidation processes required for their synthesis. Furthermore, these methods often utilize stabilizing-reducing agents such as sodium citrate or surfactants like Poly(vinylpyrrolidone) – PVP and Polyvinyl alcohol – PVA to prevent nanoparticle aggregation [6,12,13,16,17].

These procedures, while achieving high bacterial reduction, often faces limited environmental compatibility, control over nanoparticle nucleation, and industrial scalability [12–19].

Besides traditional wet chemistry treatments, physical modification techniques can also be employed: arc discharge, laser ablation, and chemical vapor deposition (CVD) offer robust anchoring of AgNPs on carbon onions and multi-walled carbon nanotubes (MWCNTs), providing hybrids with unique electromagnetic or optical properties [14,15,19]. However, these physical methods generally require specialized equipment and high energy consumption, limiting their industrial scalability.

The production and immobilization of silver nanoparticles (AgNPs) have been explored through various chemical and physical strategies, as summarized in Table S1.

In this context, we introduce a pyrrole-based dual-function molecular bridge, 2-(2,5-dimethyl-1*H*-pyrrol-1-yl)-1,3-propanediol (serinol pyrrole, SP), as a bifunctional molecule that enables the selective, mild and sustainable functionalization of sp^2 carbon substrates. The effectiveness of this approach remains consistent across different carbon morphologies, including high surface area graphite (HSAG), multi-walled carbon nanotubes (MWCNTs), and furnace carbon black (CB). Although HSAG, CNT and CB can all be seen as graphene-derived sp^2-carbon substrates, they differ in how graphene domains are organized: HSAG consists of stacked graphitic layers, CB is composed of small turbostratic graphitic packets assembled into fractal aggregates, while CNTs originate from rolled graphene sheets. Beyond geometry, these allotropes also differ in surface chemistry at the nanoscale, because real sp^2 carbons deviate from the ideal infinite polycyclic aromatic model due to topological defects, edge sites and/or curvature, which locally reduce aromatic stabilization and create chemically active regions. In CNTs, curvature intrinsically breaks planarity, whereas in HSAG and CB the presence of defects and finite graphitic domains introduces non-ideal aromatic regions and edge-like sites [20]. These features are relevant to SP anchoring because they provide local environments where cycloaddition-type reactivity (dienophile engagement) is more favorable than on a perfectly planar, defect-free graphene sheet. During this anchoring process, the methyl groups of the pyrrole ring undergo oxidation to aldehyde groups. This in situ generation of reducing sites enables the subsequent reduction of silver ions analogous to a Tollens-type mechanism promoting controlled nucleation of Ag nanoparticles directly on the carbon substrates (Figs. 1 and 2A). This bifunctional behavior underscores the generality of the approach; however, the specific morphology and surface chemistry of each carbon allotrope modulates the density and spatial distribution of anchoring/nucleation sites, leading to measurable differences in (i) Ag dispersion at the nanoscale (TEM), (ii) surface composition and Ag chemical state (XPS), and (iii) macroscopic performance (e.g., dispersion stability and antimicrobial response).

In contrast to approaches that rely on energy-intensive processing or highly specialized equipment (e.g., vacuum-based deposition, high-temperature treatments, or irradiation-assisted routes), our strategy is a molecular-bridge-enabled wet-chemical process performed under mild conditions and using standard unit operations (mixing/sonication, filtration, washing, drying). From an environmental perspective, Ag formation is achieved without external strong reducing agents and without surfactants, and it is carried out in water/ethanol with a straightforward workup. Importantly, the SP interlayer provides controlled nucleation/anchoring sites on sp^2-carbon substrates, mitigating uncontrolled Ag aggregation and improving reproducibility. Finally, the overall sequence that starts with the synthesis of the anchor molecule (SP) followed by the functionalization and Ag deposition and the washing/drying, is readily transferable to batch or continuous mixing at larger scale, supporting industrial implementation with reduced energy demand compared to physical or high-temperature methods.

This interface-driven approach yields a scalable class of silver-carbon nanohybrids with well-defined metal-carbon interactions, preserving the structural and electronic properties of the carbon phase while enabling uniform silver dispersion at low metal loadings.

2. Experimental section

2.1. Materials

2.1.1. Materials for the preparation of the adducts

HSAG Nano 307 (SA = 335–365 m^2/g, particle size distribution: 0.20–20 μm, Purity > 97%) was purchased from Asbury Graphite Mills Inc. (Kittanning, US). Chemical composition determined from elemental analysis was, as wt%: carbon 99.5, hydrogen 0.4, nitrogen 0.1, oxygen < 0.05 (Elemental analysis was performed with a Thermo FlashEA 1112 Series CHNS–O analyzer after samples were pretreated in an oven at 100 °C for 12 h). Gas sorption measurements for surface area analysis, modeled with Brunauer-Emmett-Teller (BET) theory, was determined by applying ASTM D6556 method. Resultant BET surface area of 330 m^2/g.

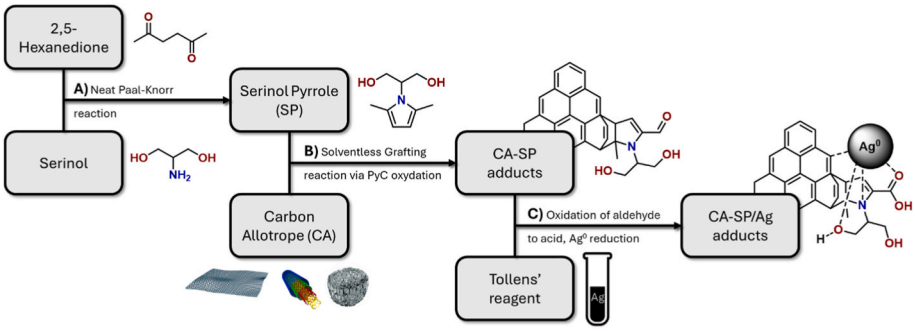

Fig. 1. Block diagrams describing (a) the reaction scheme for the neat synthesis of SP; (b) the process for the preparation of CA-SP adducts; (c) the process for the preparation of CA-SP/Ag adducts. (A colour version of this figure can be viewed online.)

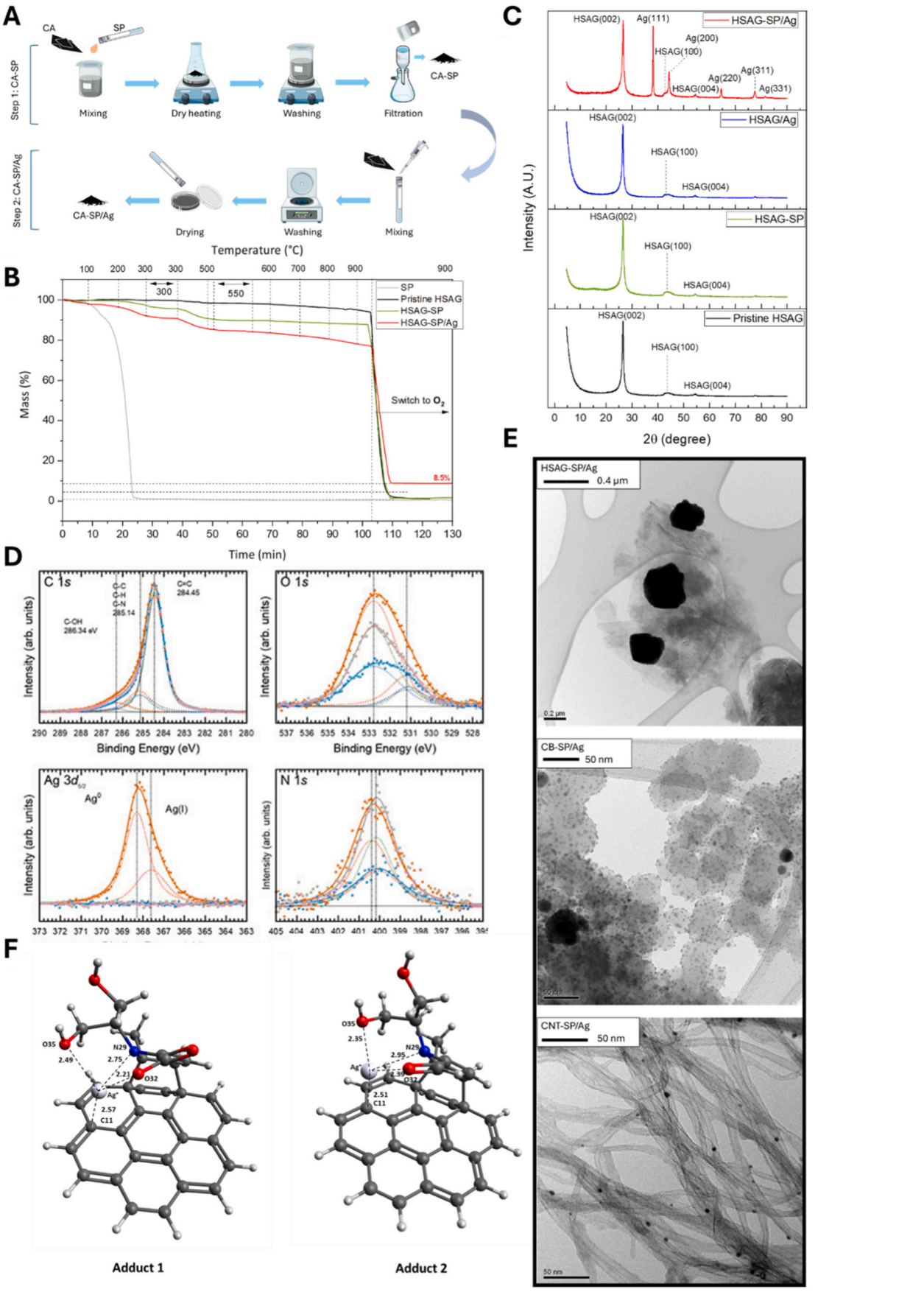

(caption on next page)

Fig. 2. Preparation and comprehensive characterization of CA-SP/Ag adducts.
(A) Process for the preparation of CA-SP/Ag adducts. Step 1: functionalization of CA with SP. Step 2. Decoration of the CA-SP adduct with Ag (created by using biorender). (B) TGA thermograms of HSAG-based adducts obtained under an inert (N_2) atmosphere, showing the weight loss profiles indicative of pyrrole functionalization and silver nanoparticle loading. (C) Wide-angle powder XRD profiles of HSAG adducts, confirming the crystalline nature of silver nanoparticles with characteristic peaks corresponding to metallic Ag. (D) XPS spectra of HSAG adducts for C 1s, O 1s, Ag 3d, and N 1s core levels. Solid lines represent the fitting of experimental data, while dashed lines are representative of their deconvolution, highlighting the successful functionalization of carbon with pyrrole and the presence of metallic silver. (E) HR-TEM images of HSAG-SP, CB-SP/Ag, and CNT-SP/Ag adducts, illustrating the uniform distribution of small silver nanoparticles (2-9 nm) on the carbon substrates and confirming the absence of large aggregates. (F) Optimized geometries of the Ag^+/adduct1–2 complex at the B3LYP/LANL2DZ level of theory. Selected bond distances are indicated in Å. The silver ion is coordinated to atoms O35, O32, N29, and C11 through non-covalent interactions. (A colour version of this figure can be viewed online.)

Multiwalled Carbon Nanotubes Nanocyl7000 (SA = 250–300 m^2/g, Average diameter = 9.5 nm, Average length = 1.5 μm, Purity = 90%) were purchased from Nanocyl (Sambreville, Belgium). BET surface area of 275 m^2/g.

Carbon Black N326 (Regal 300, SA = 78 m^2/g, Average spherical diameter = 30 nm, Purity >95%) was purchased from Cabot (Alpharetta, US). BET surface area of 77 m^2/g.

Conductive carbon black (CBc) was ENSACO 360G from Imerys (30 nm as mean diameter of spherical primary particles, BET surface area 780 $m^2\ g^{-1}$, and volume resistivity 19 Ohm × cm).

Serinol was kindly provided by Bracco (Milano, Italy). *2,5-Hexanedione* ($C_6H_{10}O_2$, MW = 114.14 g/mol) was purchased from Merck KGaA (Darmstadt, Germany). *Silver Nitrate* ($AgNO_3$, 99.9999% trace metals basis, Sigma COA, MW = 169.87 g/mol) and *Ammonia solution* (NH_4OH, 30% v/v) were purchased from Carlo Erba Reagents (Cornaredo, Italy). *Acetone* (C_3H_6O, MW = 58.08 g/mol) and Sodium Hydroxide (NaOH, MW = 39.99 g/mol) were purchased from Sigma-Aldrich (St. Louis, US). All the reagents were used as received, without any further purification and stored under dark and inert atmosphere. Distilled water (provided by Carlo Erba Reagents (Cornaredo, Italy) was always used during all the procedures.

2.1.2. Materials for the antimicrobial tests

LB broth (cod. no. L3022) and Agar powder were purchased from Merck Life Science (Milan, Italy).

E. coli JM 109 (Gram-negative bacterial strain, biosafety level 1) was purchased from Leibniz Institute DSMZ–German Collection of Microorganisms and Cell Cultures (Braunschweig, Germany).

2.1.3. Materials for the cell's viability assay

MCF-7 (HTB-22, human epithelial cells from adenocarcinoma) cell line was purchased from the American Type Culture Collection (ATCC, Manassas, VA, USA). Dulbecco's modified Eagle's medium (DMEM) and Phosphate Buffered Saline (PBS) were from Merck Life Science S.r.l. (Milan, Italy). AlamarBlue Cell Viability Assay® was purchased from Life Technologies Italia (Monza, Italy).

2.1.4. Materials for conductive inks

Serinol was kindly provided by Bracco. 2,5-hexanedione, poly(propylene glycol)-block-poly(ethylene glycol)-block-poly(propylene glycol) (PPG-PEG-PPG, Mn ~ 2.000), 1,4-butanediol, glycerol, 1,6-hexamethylene diisocyanate (HDI), propylene glycol, 2-butoxyethanol were purchased from Sigma-Aldrich. 2-(2,5-dimethyl-1*H*-pyrrol-1-yl) propan-1,3-diol (Serinol pyrrole, SP) was prepared as reported by Barbera et al. [21]. The textile substrates were a TPU from DUPONT (Intexar, TE-11C).

2.2. Preparation and characterization of CA-SP/Ag adduct

To construct multifunctional silver–carbon nanohybrids, we developed a two-step surface engineering strategy that enables precise anchoring of silver nanoparticles (AgNPs) onto sp^2 carbon allotropes via a rational pyrrole-based dual-function molecular bridge (Figs. 1 and 2A).

The process consists of the synthesis of the SP anchor molecule; the functionalization of the selected sp^2 carbon allotrope with SP; the decoration with silver using the Tollens' reagent.

2.2.1. Synthesis of the serinol pyrrole

SP chemical structure is reported in Fig. 1. SP bears two moieties with different chemical reactivities, the aromatic pyrrole ring and the glycerol moiety bearing OH groups. SP is a glycerol derivative, obtained from the Paal-Knorr reaction of 2-amino-1,3-propandiol (serinol) with 2,5-hexanedione. Glycerol is an important co-product of biodiesel production, which is one of the 15 selected structures that could be produced from a biorefinery and can be converted to value-added products through different routes, and serinol can be obtained from renewable sources as well. Also, 2,5-hexanedione can be prepared from a biobased chemical such as 2,5-dimethylfuran [22]. In brief, SP was synthesized and characterized as already reported by Barbera et al. [23,24] by mixing serinol and 2,5-hexandione and then heating the mixture at 150 °C for 3 h. The yield of the reaction, in line with the previous reports, was about 96 % and the atom efficiency was thus about 83%.

2.2.2. Functionalization of the selected sp^2 carbon allotrope

The procedure [21,25] for the preparation of adducts of SP with the selected sp^2 carbon allotrope (CA) is reported in the block diagram in Fig. 1.

Briefly, 2.00 g of CA and 0.47 g of SP were poured into a glass reaction flask, then 50 mL of acetone were added. Subsequently, the suspension was sonicated through a bath sonicator apparatus (Ultrasonic Cleaner 2200 S3, Average input power 130 W Peak ultrasonic power 260 W Power during heating 305 W, Sonica) for 20 min, then acetone was removed with a rotavapor apparatus (Rotavapor RII, BUCHI Switzerland) at 40 °C and 300 mbar. The dried sample was heated at 100 °C, then to 180 °C through a 2 -hour ramp rate heat-up under gentle mixing. 50 mL of acetone were then poured in the reaction flask and the sample kept overnight at room temperature in mixing conditions. After approximately 18 h, the sample was recovered through vacuum filtration in a Büchner funnel and the obtained powder dried (Universal Oven UNE400, Memmert) at 90 °C for 3 h. Dried powders were eventually repeatedly washed in a Soxhlet chamber with acetone at 90 °C, 16 h, dried and stored in dark environment at room temperature.

2.2.3. Decoration with silver using the Tollens' reagent

The Tollens reagent was added to generate the AgNPs on the CA-SP adduct, obtaining the Ag^+ reduction from the redox reaction with the aldehydic groups (generated from the oxidative grafting procedure reported above) of the Ag/SP adduct. The decoration procedure is detailed in the block diagram of Fig. 1.

Firstly, Tollens' reagent was prepared as follows: 1 mL of a 0.6 M $AgNO_3$ solution and 1 mL of a 2.8 M NaOH solution in distilled water were mixed in a glass vial, causing the formation of a brown precipitate; thus, NH_4OH was added dropwise until a complete precipitate dissolution was achieved. The resulting solution is Tollens' reagent.

A small aliquot of this reagent was next withdrawn and used to assess its functionality: 1 mg of glucose was transferred to a test tube, and the Tollens' reagent was added dropwise while shaking until the characteristic silver mirror appeared. The appearance of the mirror validates Tollens' reagent functionality.

The prepared Tollens' reagent was next used to functionalize our three SP-functionalized CAs (i.e HSAG-SP, CB-SP, and CNT-SP) with Ag NPs. Briefly, CA suspensions were prepared by placing 250 mg of the SP-functionalized adduct in 5 mL of H_2O in a centrifuge tube; hence, Tollens' reagent was added to the tube. 350 μL or 650 μL were added to results into adducts with different Ag loadings. The resulting solution was left in the Falcon tube for 60 min.

After that time, samples were washed twice in H_2O and a last time with acetone. Washing steps were performed by centrifuging the sample (Refrigerated Centrifuge 3-16 PK, Sigma Laborzentrifugen) at 4000 rpm for 15 min. Afterward, the supernatant was discarded, the pellet resuspended in H_2O or acetone, and the whole centrifuged again. Wet powders were next collected in a crystallizing dish and left for drying overnight at room temperature. Dried powders were eventually repeatedly washed in a Soxhlet chamber with acetone at 90 °C for 16 h, dried, and stored in a dark environment at room temperature.

2.2.4. Structural and chemical characterization of CA-SP/Ag adducts

Determination of Aldehyde Content on Graphite Surface: The concentration of surface aldehyde groups was quantified using a modified potentiometric titration method based on the oximation reaction originally proposed by Black, S. et al. [26]. This approach was selected over traditional methods for its higher precision, significantly reduced reaction time (2 h vs. 12–300 h), and the use of safer reagents.

A 0.3 N hydroxylamine hydrochloride (NH_2OH * HCl) solution was prepared by dissolving 5,75 g of NH_2OH * HCl in 250 m L of deionized water/absolute ethanol solution (50% v/v ethanol matrix). A 0.5 N triethanolamine (TEA) solution was prepared by dissolving 18,5 g of in 250 m L of deionized water/absolute ethanol solution (50% v/v ethanol).

Approximately 100–300 mg of functionalized CA-SP and CA-SP/Ag was accurately weighed into a reaction vessel. Subsequently, 2,5 mL of the 0.3 N NH_2OH * HCl solution and 2,5 mL of the 0.5 N TEA solution were added (ensuring an excess of TEA). The vessel was hermetically sealed and heated at 80 °C for 3 h under constant magnetic stirring to drive the oximation of sterically hindered aldehydic groups to completion.

After cooling to room temperature, the mixture was quantitatively filtrated and transferred to a titration beaker using aliquots of ethanol and water to maintain a 50% ethanolic environment. The excess TEA was back-titolated against a standardized 0.05 M HCl solution using a potentiometric titrator. The equivalence point was identified at approximately pH 3.4.

All analyses were performed in triplicate. A blank solution (containing NH_2OH * HCl, and TEA without CA) was prepared and treated under identical conditions to account for reagent purity and the potential formation of TEA-HCl species. The carbonyl content (C═O, in % wt/wt) was calculated as shown in Equation (1).

Titration of carbonylic groups via oximation titration.

$$C\%_{C=O} = \frac{\left(V_{blank[mL]} - V_{sample[mL]}\right) * M_{HCl} * N_{HCl} * mw_{C=O} * 100}{wt} \quad (1)$$

where V_{blank} and V_{sample} are the volumes (mL) of HCl titrant for the blank and the sample, respectively; M_{HCl} is the Molarity of the HCl solution; N_{HCl} is the titer of the HCl solution; $mw_{C=O}$ is the molecular weight of carbonyl group (28,01 g/mol) and wt is the dry weight of the graphite sample (g).

Brunauer–Emmett–Teller (BET): Nitrogen adsorption–desorption measurement was performed to investigate the specific surface area (SSA). BET surface area analysis was determined by applying the ASTM D6556 method. HSAG: 335–365 m^2/g; CNT: 250–300 m^2/g; CB: 78 m^2/g.

Thermal Gravimetric Analyses (TGA): TGA were carried out by means of a TGA/SDTA 851, Mettler Toledo AG, using the standard method ISO9924-1: a heating ramp (10 °C/min) from 30 up to 300 °C, followed by 10 min isotherm at 300 °C, then another heating ramp (20 °C/min) up to 550 °C and a subsequently 15 min isotherm at 550 °C; a final heating ramp (10 °C/min) up to 900 °C was followed by a 20 min isotherm to the end of the experiment. The whole procedure was performed in N_2 atmosphere except for the last 20 min, in which the gas in the chamber was switched to O_2.

The functionalization degree in CA-SP adducts was assessed using thermal gravimetric analyses (TGA) by quantifying the relative mass losses associated with the increasing temperature (Tables S2 and S3).

Fourier Transform Infrared Spectroscopy (FT-IR): Infrared analyses (Figs. S1–S3) were carried out by means of a Thermo Scientific Nicolet iS5 FT-IR Spectrometer, in transmission mode, deploying KBr as a dispersant media for the manufacturing of pellets. The collected data are analyzed with Thermo Scientific software OMINC.

Wide angle X-ray diffraction (WAXRD): XRD patterns were obtained in reflection, with an automatic Bruker D8 Advance diffractometer with nickel filtered Cu–K_α radiation. Patterns were recorded in 4°–90° as the 2θ range, with 2θ being the peak diffraction angle.

Raman spectroscopy: Raman spectra of powder samples deposited on a glass slide were recorded with a Horiba Jobin Yvon Labram HR800 dispersive Raman spectrometer equipped with Olympus BX41 microscope and a 50× objective. The excitation line at 532.8 nm of a He/Ne laser used for the experiments was kept at 0.5 mW in order to prevent samples degradation. Spectra were recorded as the average of four acquisitions (scan time: 30 s each) with a spectral resolution of 2 cm^{-1}.

X-ray photoelectron spectroscopy (XPS): XPS was performed in an ultra-high vacuum chamber with the base pressure of 2×10^{-10} Torr, and a non-chromatized Mg Kα source (photon energy = 1253.6 eV) at normal emission and room temperature was employed.

Photoelectrons were collected by a 150 mm hemispherical analyzer (SPECS GmbH) with a pass energy of 20 eV for high-resolution spectra and 40 eV for wide spectra. The samples were inserted in the vacuum chamber in pellet form, obtained using a manual hydraulic press. The XPS experiments were calibrated on the Ag3d5/2 core level of an Ag (111) single crystal, and no offset was applied to XPS data presented in the manuscript.

High Resolution Transmission Electron Microscopy (HRTEM): high magnification analyses were carried out with a Philips CM200, Agilent Technologies, field emission gun microscope working at an accelerating voltage of 200 kV. 1 mg/mL H_2O suspensions of samples with the highest loading of Ag (i.e. 650 μL) were prepared via mild sonication procedure through a bath sonicator apparatus, and a few drops were poured on a lacey carbon-coated film on a 200-mesh copper grid and air-dried for several hours. Low beam current densities and short acquisition times were employed. Micrographs were analyzed through ImageJ, NIH.

2.2.5. Theoretical calculations (DFT)

Molecular structures were initially built using Marvin Sketch (version 18.24, ChemAxon Ltd., Budapest, Hungary). Three-dimensional conformations were first generated using the Merck Molecular Force Field (MMFF94), followed by semiempirical optimization employing the parameterized model number 6 (PM6) Hamiltonian, as implemented in the MOPAC package (MOPAC2016 v. 18.151, Stewart Computational Chemistry, Colorado Springs, CO, USA) [27,28], prior to performing DFT calculations.

The DFT calculations were performed using the Gaussian 09 software (Gaussian, Inc., Wallingford, CT, USA) with B3LYP and LANL2DZ basis sets [29]. The LANL2DZ basis set is well-suited for describing metal–ligand interactions and is considered computationally efficient [30]. The HOMO/LUMO orbital (Figs. S11–S12) plots were obtained using the Avogadro package [31] starting from the Gaussian09 outputs. Geometry optimizations and thermal complexation energies were obtained using coronene as a model (coordinates of optimized structures in Table S7).

2.3. Antimicrobial activity and cytotoxicity of CA-SP/Ag adducts

2.3.1. Antimicrobial activity tests on CA-SP/Ag adducts

The antimicrobial activity of CA-SP/Ag (Fig. 3A) adducts was evaluated against the Gram-negative *E. coli* bacterial strain *Escherichia coli*. Tests were carried out according to the "Standard Guide for Assessment of Antimicrobial Activity Using a Time-Kill Procedure" (ASTM E2315-16) with slight modifications.

Briefly, *E. coli* bacteria were cultured in 5 mL LB broth at 37 °C under shaking at 135 rpm, until reaching an OD at $\lambda = 600$ nm (OD_{600nm}) ≈ 0.2, approximately corresponding to 10^9 bacteria/mL. Bacteria were then centrifuged and resuspended in sterile 2% (v/v) LB in H_2O, then serially diluted to reach a final concentration of 10^6 bacteria/mL (test inoculum).

HSAG, CNT, and CB samples were dispersed in sterile PBS at a concentration of 1 mg/mL and ultrasonicated (Fisherbrand Model 505 Sonic Dismembrator, Fisher Scientific) to avoid aggregation. HSAG, CNT, and CB suspensions at final concentrations ranging from 2 to 1000 mg/mL (8-fold serial dilution) were used to assess the antibacterial activity. Briefly, 400 μL of bacterial suspension were mixed with 400 μL of adduct suspensions at various concentrations into separate 2 mL-eppendorf tubes ($n \geq 3$ eppendorf/concentration/adduct type), and kept under mild rotation (8 rpm) at room temperature for 24 h. Bacterial suspension inoculated in 400 μL of PBS was used as the negative control ($n \geq 3$), whilst bacterial suspension inoculated in a 50 μM$AgNO_3$ solution was used as the positive control.

The antibacterial efficacy was evaluated after 24 h incubation by means of the plate count methods. Specifically, the number of viable bacteria was counted on LB-agar Petri dishes after serial 10-fold dilutions of the bacterial suspensions and plating.

2.3.2. Cellular viability assay on CA-SP/Ag adducts

To assess the in vitro cytotoxicity of/adducts to MCF-7 cells, indirect cytotoxicity tests were performed according to the ISO 10993-5 standard norm, with slight modifications (Fig. 3B).

Mycoplasma-free MCF-7 cells were cultured in Dulbecco's Modified Eagle's Medium (DMEM), supplemented with 10% (v/v) fetal bovine serum (FBS), 1 mM sodium pyruvate, 10 mM HEPES, 100 U/mL penicillin, 0.1 mg/mL streptomycin and 2 mM glutamine (hereinafter referred to as complete DMEM, cDMEM).

Cells were plated at 10^4 cells per well in 96-well plates and cultured in a solution of 90% (v/v) of cDMEM 10% (v/v) and PBS for 24 °C at 37° in a humidified atmosphere under constant supply of 5% (v/v) CO_2 (hereafter referred to as standard culture conditions).

Following 24 h incubation, cells were challenged with 100 μL of CA-SP/Ag adducts dispersions prepared at different concentrations, namely MBC and supra-MBC (10× MBC), then incubated under standard culture conditions for 24 h. Cells cultured in fresh medium served as the negative control for the experiment, while cells challenged with 250 μM $AgNO_3$ solution were used as a positive control for cytotoxicity.

Following 24 h incubation, cells were washed with warm, sterile PBS, then detached from wells with Trypsin/EDTA solution and counted using Trypan Blue. Cell viability was evaluated as follows (equation (2)).

Evaluation of the cytotoxicity of adducts.

$$cytotoxicity\ (\%) = 100\% - viability\ (\%) = \left(1 - \frac{\#viable\ cells_{sample}}{\#viable\ cells_{CTRL}}\right) \quad (2)$$

2.4. Scalable, high shear mixing (HSM), production of HSAG-SP/Ag

Using a Silverson L5M-A mixer, a high shear mixing (HSM) system [32], deployed also at industrial level, the two-step synthesis of HSAG–SP/Ag nanohybrids (Fig. 3C) were translated in a one-pot process. The high shear mixing setup selected was: rotor diameter $D = 32$ mm, rotor/stator spacing of 120 μm and squared holes high shear screen.

The synthesis of the HSAG-SP/Ag (HSM) adduct was conducted as follows: 300 mg of SP were poured in a 250 mL beaker and solubilized in 100 mL of distilled water. Then 3.00 g of HSAG were added. In the first step, the suspension was concurrently heated at 80 °C on a heating plate and mixed at 5700 rpm using Silverson L5A-M HSM for 90 min. After 90 min the heated plate had been switched off, and the mixing was stopped. In the second step, Tollens' reagent was added once the temperature decreased below 35 °C. The suspension was mixed for 20 min at 2000 rpm at ambient temperature (20 ± 3 °C). The suspension was next collected in a crystallizing dish and left for drying at 90 °C for 16 h. Dried powders were eventually repeatedly washed in a Soxhlet chamber with acetone at 90 °C for 16 h, dried, and stored in a dark environment at room temperature. The resulting synthesized adducts were analyzed by means of TGA, XRD and TEM (Figs. 3D, E and S1A, B).

2.5. Antimicrobial activity tests on coatings containing CA-SP/Ag adducts

Antibacterial tests were performed according to the ISO 22196:2011, with slight modifications.

E. coli JM109 were cultured in 5 mL of LB broth at 37 °C under shaking at 135 rpm until reaching an OD (Optical Density) at $\lambda = 600$ nm (OD600nm) ≈ 0.2, approximately corresponding to 10^9 bacteria/mL. The bacterial suspension was then centrifuged, and the pellet was resuspended in 10% (v/v) MilliQ in LB. This suspension was diluted to reach the desired microbial concentration of 10^6 bacteria/mL (hereinafter referred to as the test inoculum).

Afterward, 40 μL drops of the test inoculum were dispensed on the surface of each test specimen. Squared (18 × 18 mm, 324 mm^2) glass coverslips (previously sterilized) were next applied on the drops to maximize the contact between bacteria and the surface. Desired microbial concentration on the surface of the test specimens was 1.5×10^4 CFU/cm^2. Inoculated test specimens were next incubated at a temperature of 37 °C and 90% RH for 24 h.

Following 24 h-incubation, bacteria were recovered from the surfaces of test specimens by adding 1 mL (V_1) of SCDLP broth (Soybean Casein Digest with Lecithin and Polyoxyethilene Sorbitan Monooleate). Then, 30 μL (V_2) of the mix of SCDLP and bacteria were next removed from the surface of test specimens, serially diluted and plated on separate LB-agar plates. Plates were then incubated for 24 h at 37 °C and 90% RH. The number of CFU grown in the plates was obtained by a visual examination.

All conditions for considering the test valid according to ISO norm 22,196:2011(E) were satisfied.

The number of viable bacteria recovered from each test specimen was obtained by the following equation (equation (3)).

Calculation of the number of viable bacteria.

$$N = \frac{\left(C \times D \times \frac{V_1}{V_2}\right)}{A} \quad (3)$$

where N is the number of viable bacteria recovered per cm^2 of test specimen; C is the average plate count for the duplicate plates; D is the dilution factor for the plates counted. V_1 is the volume, in ml, of SCDLP added to the specimen; V_2 is the volume, in ml, of the mix of SCDLP/recovered bacteria withdrawn from the specimen and plated; A is the surface area, in cm^2, of the cover film.

2.5.1. Antimicrobial PVA-composite materials

The applicability of the HSAG-SP/Ag as an antimicrobial adduct was evaluated by using it as an active antibacterial agent for biocidal surfaces. The adduct was mixed into a commercially available PVA-based polymer formulation, and homogeneous surfaces were obtained (Fig. 4A) Different PVA composites were prepared to assess the positive function of AgNPs.

PVA. 16 mL of distilled water and 0.80 mL of propylene glycol were added. The suspension was sonicated through a bath sonicator

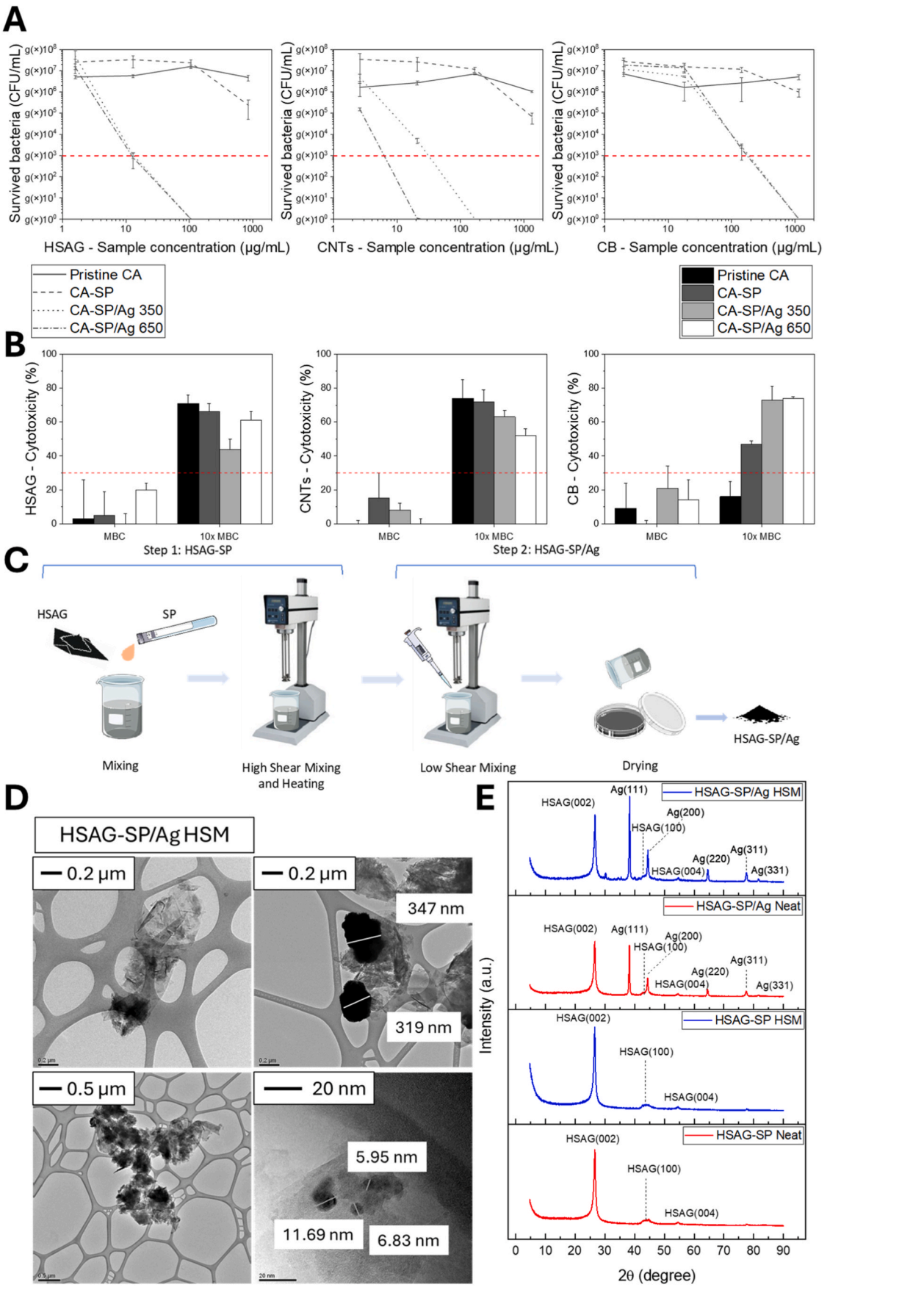

(caption on next page)

Fig. 3. Antimicrobial efficacy and scalable production of CA-SP/Ag nanocomposites. (A) Antimicrobial efficacy of Ag-adducts, expressed as the number of surviving bacteria [CFU/mL] as a function of adduct concentration [μg/mL] in liquid media. The dose-response curves demonstrate the effectiveness of the adducts, with a clear reduction in bacterial viability as the concentration increases. The minimal bactericidal concentration (MBC) is indicated, reflecting the lowest concentration at which a 99.99% reduction in bacterial load is achieved. (B) Cytotoxicity of CA/Ag adducts. The MBC group corresponds to the concentration determined to be the minimal bactericidal concentration from antimicrobial assays. The 10 × MBC group represents a concentration ten times higher than the estimated MBC, showing the effect on cell viability at supra-MBC levels. The results indicate that the adducts show minimal cytotoxicity at MBC concentrations, suggesting biocompatibility for potential applications. (C) Schematic representation of the synthesis process for HSAG-SP/Ag adducts through HSM-mediated functionalization (created by using biorender). (D) HR-TEM micrographs of synthesized HSAG-SP/Ag adducts. (E) Powder wide-angle XRD profiles of HSAG-SP-based materials, comparing pristine (neat) and Ag-functionalized adducts obtained via HSM (blue) and the conventional production process (red): The presence of metallic silver can be easily observed also on HSM preparations. (For interpretation of the references to colour in this figure legend, the reader is referred to the Web version of this article.)

apparatus (Ultrasonic Cleaner 2200 S3, Sonica) for 10 min, then 2 mL of a PVA emulsion were added. The mixture was magnetically stirred at room temperature for 2 h then approximately 5 mL of dispersion were transferred in a Petri plate and left for drying at room temperature for 48 h. Specimens were next heated at 80 °C for 2 h to enable curing of the matrix.

PVA + HSAG: 0.80 g of pristine HSAG were weighed in a beaker, and 16 mL of distilled water and 0.80 mL of propylene glycol were added. The suspension was sonicated through a bath sonicator apparatus (Ultrasonic Cleaner 2200 S3, Sonica) for 10 min, then 2 mL of a PVA emulsion were added. The mixture was magnetically stirred at room temperature for 2 h then approximately 5 mL of dispersion were transferred to a Petri plate and left for drying at room temperature for 48 h. Specimens were next heated at 80 °C for 2 h to enable curing of the matrix.

PVA + HSAG-SP: 0.80 g of pristine HSAG-SP were weighed in a beaker; 16 mL of distilled water and 0.80 mL of propylene glycol were added. The suspension was sonicated through a bath sonicator apparatus (Ultrasonic Cleaner 2200 S3, Sonica) for 10 min, then 2 mL of a PVA emulsion were added. The mixture was magnetically stirred at room temperature for 2 h, then approximately 5 mL of dispersion were transferred to a Petri plate and left for drying at room temperature for 48 h. Specimens were next heated at 80 °C for 2 h to enable curing of the matrix.

PVA + HSAG-SP/Ag: 0.80 g of pristine HSAG-SP/Ag were weighed in a beaker; 16 mL of distilled water and 0.80 mL of propylene glycol were added. The suspension was sonicated through a bath sonicator apparatus (Ultrasonic Cleaner 2200 S3, Sonica) for 10 min, then 2 mL of a PVA emulsion were added. The mixture was magnetically stirred at room temperature for 2 h, then approximately 5 mL of dispersion were transferred to a Petri plate and left for drying at room temperature for 48 h. Specimens were next heated at 80 °C for 2 h to enable curing of the matrix.

2.6. Conductive ink printed on flexible substrates for electronic applications

A two-component system was developed, consisting of a pre-ink and a polyurethane-based adhesive, printed on a Thermoplastic polyurethane (TPU) substrate commonly used in electronics. The adhesive was prepared as previously described by some authors [33]. Conductive fillers used in the ink were conductive carbon black (CBc) and silver flakes (<10 μm), as well as CBc functionalized with serinol pyrrole (SP) and decorated with silver nanoparticles (AgNPs).

Filler concentrations were set at 10% (w/w to the adhesive matrix) for carbon-based inks and 70% for silver flakes-based ink to ensure good dispersion and printability. The components were homogenized using a planetary centrifugal mixer and printed with a bar coater. After oven curing, the ink layers reached a thickness of about 10 μm.

2.6.1. Electrical characterization of silver – decorated CA-based inks

Electrical resistance was measured using a multimeter, Keysight 34450 A 5 ½ – digit multimeter with OLED display. This instrument's performance accuracy is 0.015% DCV. The setup (Fig. S13) is used for the measurement of sheet resistance of thin films and coating layers and imposes the width of electrodes to be equal to the distance between electrodes.

The copper electrodes of the employed device present a hole on the upper surface to hold multimeter probes in place, while the bottom side of the electrodes is flat and is directly positioned on the material.

Sheet resistance values are reported in Table S11.

3. Results and discussion

3.1. Preparation and characterization of CA-SP/Ag adduct

The pyrrole molecule orchestrates a two-step cascade reaction: first, it covalently binds to the carbon surface via thermal cycloaddition; then, its aldehydic moiety drives in situ Ag^+ reduction and nanoparticle nucleation. In particular, in the first step, a serinol-derived pyrrole (SP) was covalently grafted onto sp^2 carbon allotropes (CAs) via a high-temperature Diels-Alder cycloaddition [23,24]. Upon thermal activation, aldehyde groups emerged on the SP moiety, enabling a Tollens-type redox reaction that reduces Ag^+ ions in situ, yielding uniformly distributed Ag nanoparticles (AgNPs) directly on the carbon surface [25].

This strategy avoids external reductants and surfactants, resulting in Ag-CA adducts with SP coverage ranging from 4.4 to 9.7 wt% and Ag loading between 7.9 and 13.1 wt% (Tables S2 and S3). Characterization via FT-IR, TGA, XRD, XPS, RAMAN, and HR-TEM confirmed the presence of metallic Ag (2–9 nm), covalent SP anchoring, and controlled nanoparticle nucleation (Figs. 2B–E and S1–S9). Larger aggregates (100–400 nm) were observed in HSAG samples, attributed to edge functionalization and localized Ag^+ concentration, consistent with the LaMer model [34,35]. Control experiments on non-functionalized CAs yielded negligible Ag deposition, validating the dual role of SP: aldehyde-driven reduction and anchoring via organic functionalities. The cascade mechanism was further supported by increased oxygen content (O1s) and organic species in XPS spectra post-functionalization.

Characterization results, in particular thermogravimetric analysis (TGA) (Fig. 2B), show a SP functionalization in the range of 4.4–9.7 wt% and Ag loading between 7.9 and 13.1 wt% across different carbon allotropes (Tables S2 and S3). Other analyses, such as FT-IR, XRD, XPS and HR-TEM, as depicted in Fig. 2C, D confirm the surface chemistry and reaction mechanism.

FT-IR spectroscopy (Figs. S1–S3) confirms the presence of the absorption bands relating to the presence of the organic molecule and its binding. In particular, for HSAG-SP adducts, but also similarly to the other carbon allotropes, organic moiety signals can be identified around 2900 cm^{-1} (represented by the C–H stretching) and around 1550 cm^{-1} for C–O signals and 1250, 1050, 800 cm^{-1} by means of C–N and C–H signals. Notably, the fingerprint signal at 800–750 cm^{-1} serves as a pivotal diagnostic peak: it is associated with the Out-Of-Plane (OOPLA) bending signals typical of aromatic ring pyrrole's C–H groups [24]. Since Tollens' reagent oxidizes aldehydic groups to carboxylates, the disappearance of characteristic IR bands serves as a reliable diagnostic tool. Specifically, the reaction is confirmed by the depletion of the C═O stretching band, particularly clear for HSAG, at approximately 1600 cm^{-1}. No other differences were recorded for silver – decorated allotropes, as metallic silver shows no IR absorption bands.

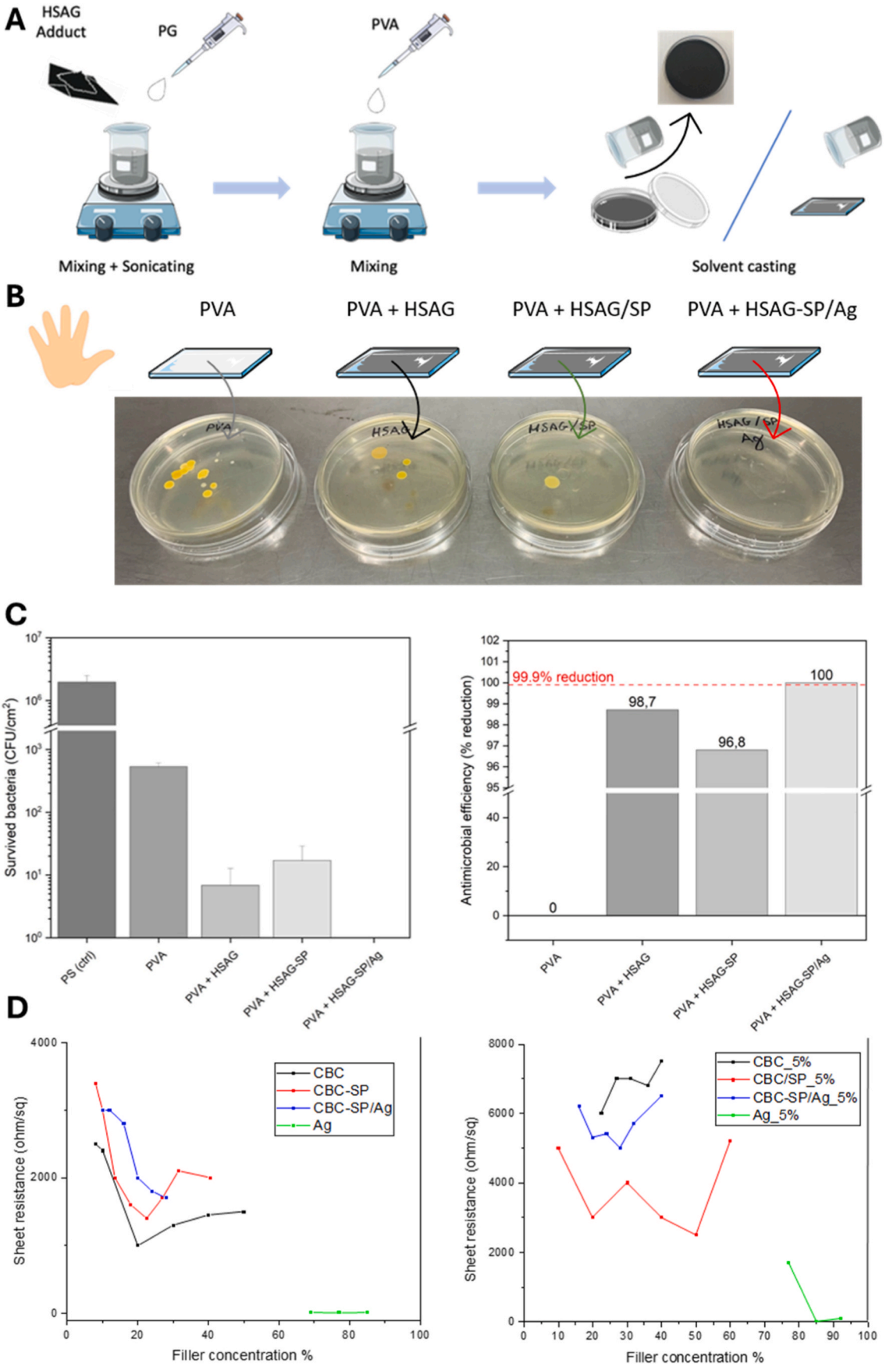

(caption on next page)

Fig. 4. Assessment of the antimicrobial and conductivity properties of composite materials incorporating the HSAG-SP/Ag adduct. (A) Schematic representation of the fabrication process for HSAG-SP/Ag-integrated composite materials (created by using biorender). (B) Results from the surface hand-touch assay, where bacterial colonies in Petri dishes indicate the survival of microorganisms transferred from the hands of three randomly selected individuals onto the composite coatings, following exposure to their biocidal action. The results show a significant reduction in bacterial growth on treated surfaces, confirming the antimicrobial efficacy of the composite materials. (C) Antimicrobial performance evaluation based on ISO 22196, the standard method for determining antibacterial activity on non-porous plastic surfaces. Results are presented as "Surviving bacteria [CFU/cm^2]" (left) and "Antimicrobial efficiency [% reduction relative to the reference material (PVA)]" (right), demonstrating the superior antibacterial performance of the HSAG-SP/Ag composite, which achieved over 99.9% bacterial reduction compared to the reference material (PVA). (D) Sheet resistance of CBc, CBc-SP, CBc-SP/Ag, and Ag flakes inks at rest (left) and under 5% strain (right). At rest, the pristine structure of CBc allowed to reach a lower sheet resistance compared to the modified CBc. A correlation between increasing filler concentration and decreasing resistance under strain is observed with functionalized filler and filler loadings <20 wt%. At higher concentrations, the matrix fraction was not effective in maintaining the network efficient under deformation, leading to lower electrical performance. In contrast, the presence of the lone pristine CBC, without SP functional groups, leads to an immediate network failure under stretching even at low filler concentration. Under stretching, the SP moieties promoted better interaction with the matrix, promoting filler networking, and thus conductivity. In particular, the CBc-SP/Ag formulation exhibited better properties compared to CBc alone, introducing silver, while maintaining a significantly lower filler concentration than pure Ag flakes inks. (A colour version of this figure can be viewed online.)

In addition to the FTIR analyses, a potentiometric titration of the aldehyde groups present on the functionalized carbon allotropes was performed. Pristine, non-functionalized allotropes were employed as blanks under identical experimental conditions. The results, reported in the following Table 1, show a clear decrease in aldehyde content after the reaction, consistent with aldehyde consumption during Ag^+ reduction. Pristine CA carbonyl content was measured and subtracted for a more precise measurement.

The metallic nature of Ag was confirmed by XRD analyses showing the characteristic peaks of the crystal lattice of Ag NPs, i.e., Ag (111), Ag (200), Ag (220), Ag (311), and Ag (331) (Figs. 2d, S5 and S6).

XPS analysis (Figs. 2D, S7 and S8), particularly the C1s, reveals π-rich graphitic backbones; the O1s, reveals hydroxyl and carbonyl residues; and N1s spectra, confirm the presence of covalently bonded pyrrole onto the carbon allotrope surface. The presence of metallic silver is also confirmed by the Ag3d$_{5/2}$ spectra: only a very few Ag^+ can be detected, ensuring that the reduction reaction, driven by aldehydic groups on the pyrrole compounds, has taken place.

More specifically, in the XPS wide scan spectrum of HSAG-SP, HSAG-SP/Ag, and the control experiment HSAG-Ag, four signals were searched for: C1s, O1s, N1s, and Ag3$d_{5/2}$.

In HSAG-SP, C1s, O1s, and N1s are detected. In particular, the carbon signal was deconvoluted (C1S), detecting three interesting components (Fig. 2D). One peak has the same position as that of graphite (284.45 eV), with the characteristic tailing on the high energy side, due to the π bond shake-up satellite, which is clear in the HSAG spectrum. The other two components of C1s are found at higher binding energies, due to the electron-withdrawing effect of oxygen. They are attributable to C–O (285.2–285.7 eV) and C═O (286.34 eV) functionalities. The presence of oxidized groups is further confirmed by the O1s XPS line shape (Fig. 2D). It should be noted that XPS analyses only examine the exterior layer (about 40 Å thick) of the graphitic material; therefore, O1s spectra may also be more surface-specific than C1s. There are two main contributions to the O1s signal, i.e., at 531.3 eV and at 532.8 eV. Based on the literature data, the signal at 531.3 eV can be attributed to the C═O vibrations of carbonyl groups (it accounts for around 30% of the signal intensity). The component at 532.8 eV provides evidence for the presence of C–O groups identified as hydroxyl (it accounts for around 70% of the signal intensity). The contribution could account for OH groups on the propanediol moiety.

The most frequently assigned N1s peaks are pyridine (398.2–399.1 eV) [36], graphitic-N (401.1–402.7 eV) [36], nitric oxide (402.6 eV) [36], amine (400.0 eV) [37] and pyrrolic (400.4 eV) [38].

In particular, the shift of the N1s peak centre from 400.2 eV (HSAG-SP) to 400.4 eV (HSAG-SP/Ag) suggests the presence of aliphatic systems. These data support the formation of the covalent adduct of Diels-Alder since the pyrrole, once reacted, loses its aromaticity.

The last signal to be analyzed is the one due to silver. This signal is detectable only in the HSAG-SP/Ag adduct. For HSAG-SP/Ag, there are two main contributions to the Ag3$d_{5/2}$ signal, namely at 367.6 eV and 368.3 eV. Based on literature data, the signal at 367.6 eV can be attributed to Ag(I) and that at 368.3 eV to Ag(0). All the CA-SP/Ag hybrids were analyzed by means of XPS, confirming results observed on the HSAG-SP/Ag adduct (Figs. S67 and S8). In the case of the control experiment, only C1s, O1s, and N1s were detected. The absence of the silver signal confirms the determining role of the oxidized pyrrole function. A small amount of reduced silver is detectable on CNT not functionalized with the organic moiety. This aspect seems to be related to the presence of carbonyl groups on the pristine carbon nanotubes, confirmed by the presence of O1s, in the XPS spectrum (Fig. S8).

Raman spectroscopy further supports SP functionalization on sp^2-carbon substrates. For HSAG, CNT and CB [39], SP-functionalized samples exhibit higher I_D/I_G ratios and a related decrease of the L_a [nm] dimension of the crystallite, calculated trough Tuinstra and Koenig equation (4), where C(λ) = 19.22 nm for a 532 nm laser [40], compared to pristine materials (Fig. S4; Table S4), consistent with the introduction of sp^2 defects/disorder upon covalent modification and in line with previous reports [41,42] on pyrrole-based functionalization.

Tuinstra and Koenig equation for the calculation of crystallite dimension.

$$L_{a[nm]} = C(\lambda)/I_D/I_G \quad (4)$$

TEM images, coupled with Selected area electron diffraction – SAED, focusing on electron-dense spots highlighted AgNPs formation within each allotrope (Figs. 2E and S9). For each case the diameter of AgNP was calculated to be in the range from 2 to 9 nm. Bigger aggregates (~100–400 nm) were found in HSAG samples, presumably indicating local aggregation phenomena. We suggest this result be attributed to the characteristic edge-functionalization of HSAG: edge-functionalization promotes local increase of Ag NPs concentration on these edges; hence, nucleation occurs to a higher extent according to the Lamer model [43,44]. We hypothesize that edge functionalization promotes the formation of locally high concentrations of metallic Ag, which hence grows in bigger aggregates.

A control Tollens' test was also performed on the non-functionalized allotrope, revealing very low levels of silver from both XRD and XPS analyses (Fig. 2C and D) and confirming the working hypothesis consisting of the double role of the organic portion: 1. The aldehyde reacts by oxidizing and determining the reduction of silver, which is in; 2. Finds in the organic functionalities present, an anchor for the growth of the nanoparticles. This cascade reaction, with the formation of a double-oxidized SP species, is supported by results from TGA, which reports data in line with the amount of pyrrole compound and silver grafted

Table 1
Potentiometric titration results for all the carbon allotropes. Aldehyde total content (mg/mg CA) has been reported. Data are reported as mean ± SD $\%_{wt/wt}$C=O.

	Pristine CA	CA-SP	CA-SP/Ag
CB	0,07 ± 0,02	1,48 ± 0,03	0,19 ± 0,02
HSAG	0,10 ± 0,04	1,24 ± 0,04	0,28 ± 0,03
CNTs	0,15 ± 0,04	1,40 ± 0,02	0,16 ± 0,03

onto the allotropes, and XPS analyses, revealing a higher content of organic species and oxygen (O1s) after Ag functionalization, respectively.

Density Functional Theory (DFT) shows that the carboxylate adduct 1 binds Ag^+ much more strongly and with a clearer tetrahedral motif than the aldehyde adduct 2 (Fig. 2F); upon reduction to Ag^0 the interaction energies become similar, indicating the framework remains essentially unchanged. WBI/NBO analyses identify oxygen lone pairs as the dominant stabilizing donors, with the strongest contribution in adduct 1, while frontier orbitals place acceptor character on the Ag^+ site. Overall, the carboxylate group is the key stabilizing element, making adduct 1 about 33 kcal/mol more stable than adduct 2. Overall, the carboxylate functionality is the key stabilizing element, making adduct 1 about 33 kcal/mol more stable than adduct 2 and supporting Ag^+ chelation prior to Ag^0 growth (Details are reported in S3).

3.2. Antimicrobial activity and cytotoxicity of CA-SP/Ag adducts

The antimicrobial efficacy of CA-SP/Ag adducts was systematically assessed in a liquid environment against *Escherichia coli*. Here, adducts were prepared using two different volumes of Tollens' reagent for each to test differences in biocidal behavior caused by a variation in the Ag loading.

The bactericidal effect associated with the presence of silver nanoparticles supported on sp^2 carbon substrates exhibits a dose-dependent response, as shown in Fig. 3A. Dose-response curves for the three CAs show earlier inflection points for HSAG and CNT-based adducts, indicating higher antimicrobial efficacy compared to CB-based adducts. The minimal bactericidal concentration (MBC) was determined for each of the three CAs using a 99.99% reduction in bacterial load as the threshold criterion, as detailed in Table S10. A discernible trend in MBC values was observed, with HSAG exhibiting the lowest value of MBC (7-9 μg/mL), followed by CNT (7-23 μg/mL) and CB (180-195 μg/mL). These findings suggest an inverse correlation between the MBC of the adducts and their specific surface area, where a larger interfacial area between the nanomaterial and bacterial cells enhances antimicrobial activity.

Subsequently, the cytotoxicity of the synthesized adducts was evaluated against eukaryotic cell lines, specifically MCF7 murine fibroblasts. To this purpose, adducts were resuspended in selected media at their respective MBC values, and their impact on cellular viability was assessed by trypan-positive cell count. Notably, at such concentrations, no significant cytotoxic effect was observed, as evidenced by a mortality rate below 30% (Fig. 3A). Using a ten-fold higher concentration of adducts, potential cytotoxicity was additionally probed at supra-MBC levels. While cytotoxicity increased beyond this threshold, the mortality rate of MCF fibroblasts did not exceed 80% (Fig. 3B).

Overall, these results underscore a remarkable antibacterial activity of Ag-containing adducts, particularly those based on HSAG and CNT substrates. Simultaneously, these adducts exhibit negligible cytotoxicity at their MBC values, highlighting their potential as effective antimicrobial agents with minimal adverse effects on eukaryotic cells.

3.3. Scalable, high shear mixing (HSM), production of HSAG-SP/Ag

To promote the scale up and the sustainability of a process for the synthesis of the sp^2 carbon allotropes' adducts with SP, the preparation of HSAG-SP adduct was carried out in water, by using a high-shear mixer (HSM) [32], available at the industrial level, in a one pot process, schematized in Fig. 3C. In particular, SP grafting occurred at 80 °C for 90 min, under 5700 rpm stirring. Ag atoms were then anchored, which gave rise to AgNP growth at room temperature for 20 min, under 2000 rpm stirring. The functionalization of HSAG with SP favored the formation of stable water dispersions, as shown in Fig. S10B.

To better understand and optimize the process parameters, a theoretical model was employed where exfoliation of HSAG is modeled as shear-induced intermonolayer sliding in a solvent [45,46].

The minimum shear rate ($\dot{\gamma}$) required to initiate the separation (destacking) of graphite layers was calculated using the following equation (5).

Approximative minimum shear rate for the exfoliation of HSAG.

$$\dot{\gamma} = \left(\sqrt{(\{E\_S, G\})} - \sqrt{(\{E\_S, L\})}\right)\hat{1}/\eta L \approx 6.4 \cdot 10\hat{4}\ m/s \quad (5)$$

The calculated result of approximately 6.4 ·10ˆ4 m/s was derived using the difference between the square roots of the surface energy of graphite ($E_{S,G} \approx 60$ mJ/m^2) and the surface energy of the liquid ($E_{S,L} \approx 72$ mJ/m^2 for water), normalized by the liquid viscosity (η) and the flake length (L). This formulation highlights the critical dependency of the required shear rate on the energetic match between the solid and the solvent.

Subsequently, Equation (6) was used to translate the necessary shear rate ($\dot{\gamma}$) into the minimum rotational frequency in Revolutions Per Minute (RPM) for the specific high-shear mixer configuration.

Minimum speed for achieving proper exfoliation of HSAG.

$$\dot{\gamma} = \pi ND/\Delta R \approx 4500\ RPM \quad (6)$$

In this context, $\dot{\gamma}$ is calculated based on the rotational frequency (N) of the rotor, its diameter (D), and the rotor/stator distance (ΔR) (gap size). The resulting value of approximately 4500 RPM thus represents the estimated minimum rotational speed required to achieve the destacking of the graphite flakes in water using the high-shear Silverson mixer.

The reproducibility of the synthesized adduct was assessed through TEM and TGA analyses (Figs. 3D, E, S10A and Table S5): the HSM-derived nanohybrids were similar to those prepared with the high temperature neat process. More particularly, the X-ray Diffraction (XRD) analysis confirmed changes in the material's structure following treatment. Focus was placed on the characteristic (002) reflection for the HSAG material, as this peak directly relates to the *c*-axis stacking order and interlayer spacing (d_{002}).

Utilizing the full width at half maximum (FWHM) of the (002) peak, the average coherent scattering domain size (L_c) was calculated using the Scherrer equation (Equation (7)). For highly ordered graphitic sheets, this value can be related to the number of stacked layers (N), providing an estimate of the crystalline stacking order.

The Scherrer equation that correlates crystallinity and number of layers.

$$Lc = K\lambda \backslash \beta\ cos\ \theta \quad (7)$$

Analysis of the peak profile revealed a slight decrease in the average crystallite thickness. Quantitatively, the number of stacked layers reduced from 22 to 20, indicating a minor degree of exfoliation or structural modification under the adopted experimental conditions. Graphite suspensions, prepared using the same High Shear Mixing procedure, were compared to assess their long-term stability. A centrifugation test was performed: at 1000 RPM, HSAG-SP showed stability even after 1 h of centrifugation, in contrast to pristine which sedimented after 15 min of centrifuging (Fig. S10B). Correlated behavior was observed also with a time-depending decantation test. The non-functionalized graphite sedimented almost completely within 5 days. Conversely, functionalization with SP conferred great stability, allowing the HSAG-SP graphite to maintain a homogeneous suspension after the same period (Fig. S10C).

These analyses confirmed that both the degree of functionalization and the crystallinity of the HSAG-SP/Ag (HSM) adduct were preserved in comparison to adducts synthesized via the conventional neat procedure. Collectively, these findings support the feasibility of scaling up the production of the HSAG-SP/Ag adduct using industrial-scale HSM systems.

3.4. Dual functionality: CA-SP/Ag based coatings as antimicrobial and conductive adducts

The multifunctionality of the CA-SP/Ag nanohybrids was demonstrated through two high-impact applications: antimicrobial polymeric coatings and flexible conductive inks. These implementations not only validate the dual performance of the material but also address pressing global needs in public health and sustainable electronics (Fig. 4).

3.4.1. Antimicrobial activity tests on coatings containing CA-SP/Ag adducts

The antibacterial activity of these surfaces was next evaluated both following the ISO 22196:2011 standard for assessing the antibacterial activity of non-porous plastic surfaces, with some minor technical variations, and with a practical test involving hand-touching samples and monitoring the residual bacterial charge on the tested surfaces (Fig. 4A). The tests demonstrated excellent transfer of antibacterial properties from the adduct to the composite surface, with a bacterial reduction of at least 99.9% for the Ag-HSAG-SP + PVA surface (Fig. 4B and C). These results show that the Ag-HSAG-SP adduct can be used as an antibacterial agent in formulations for the preparation of antibacterial composite materials.

3.4.2. Printable conductive inks

To explore suitability for piezoresistive sensors, stretchability tests were conducted using CBc-based inks. It is crucial to match not only the solubility parameter with the polyurethane matrix but also to maintain a continuous network during deformation.

Resistance changes for pristine CBc, CBc-SP, and CBc-SP/Ag inks printed on stretchable TPU are shown in Figs. 4D and S13. As shown in Table S11, functionalization improved the conductive network under strain, lowering sheet resistance within typical concentrations (<30%). CBc-SP/Ag also exhibited better dispersion; free SP groups interacted with the matrix, supporting a stable network – a phenomenon analogous to the Payne effect observed in tire composites, where the dynamic strain dependence of the storage modulus is reduced by improved filler-polymer interactions. This functionalization helps to keep electrical properties under stretching at lower filler content, unlike silver-based inks which require >75% (w/w) of filler concentration to maintain conductivity under strain.

Crucially, the synergy between SP and Ag enables conductivity and antimicrobial protection at drastically reduced silver loadings, addressing a major bottleneck in the development of sustainable electronic materials. Traditional silver-based inks rely on high metal content to achieve performance, resulting in elevated costs, resource dependency, and environmental concerns. In contrast, our SP-interface-engineered nanohybrid achieve comparable or superior functionality with minimal Ag content, unlocking a material-efficient route to stretchable, biocidal electronics.

4. Conclusions

In this work, we demonstrated how molecular interface engineering can be used to integrate antimicrobial functionality and electrical conductivity in silver-carbon hybrid materials through a scalable and environmentally compatible approach. By exploiting a pyrrole-based dual-function molecular bridge, we developed a rational strategy for the selective functionalization of sp^2 carbon allotropes, enabling simultaneous covalent anchoring to the carbon surface and controlled in situ nucleation of silver nanoparticles under mild, surfactant-free conditions.

Comprehensive physicochemical characterization confirmed the formation of uniformly distributed Ag nanoparticles with controlled morphology and strong metal-carbon interactions, while preserving the structural and electronic properties of the carbon substrates. Importantly, the functionalization protocol was successfully translated to an aqueous high-shear mixing process, demonstrating industrially relevant scalability without loss of performance.

The resulting Ag-carbon nanohybrids exhibited strong antibacterial activity, with minimum bactericidal concentrations as low as 7-9 μg/mL for HSAG-based adducts and low cytotoxicity toward eukaryotic cells. When incorporated into polymeric coatings and conductive inks, the materials retained electrical conductivity under mechanical deformation and displayed enhanced piezoresistive behavior at significantly reduced silver loadings.

Overall, this study provides a general and scalable interface-driven route for the preparation of silver-carbon nanohybrids with controlled structure and multifunctional performance. The proposed molecular-bridge-enabled functionalization strategy offers a versatile platform for the development of carbon-based materials where surface chemistry, processability, and functional integration must be simultaneously addressed.

CRediT authorship contribution statement

Edoardo Testa: Writing – review & editing, Writing – original draft, Validation, Software, Formal analysis. **Simone Raciti:** Writing – original draft, Formal analysis. **Davide Gentile:** Writing – review & editing, Writing – original draft, Visualization, Software, Methodology, Formal analysis, Data curation, Conceptualization. **Mattia Mondella:** Formal analysis. **Francesco Goto:** Writing – review & editing, Writing – original draft, Investigation, Formal analysis, Data curation. **Gianlorenzo Bussetti:** Writing – review & editing, Validation, Supervision, Resources, Methodology, Investigation, Data curation. **Nina Bono:** Writing – review & editing, Writing – original draft, Validation, Supervision, Investigation, Data curation. **Dario Allevi:** Writing – review & editing, Writing – original draft, Validation, Formal analysis. **Alberto Bottari:** Writing – review & editing, Writing – original draft, Formal analysis. **Gabriele Candiani:** Writing – review & editing, Supervision, Resources, Project administration, Investigation, Data curation. **Maurizio Galimberti:** Writing – review & editing, Writing – original draft, Validation, Resources, Methodology, Data curation. **Vincenzina Barbera:** Writing – review & editing, Writing – original draft, Validation, Supervision, Resources, Project administration, Methodology, Investigation, Funding acquisition, Data curation, Conceptualization.

Data availability statement

All data supporting the findings of this study, including raw and processed experimental datasets (thermogravimetric analysis, XRD, XPS, HR-TEM, FT-IR, SAED), antimicrobial and cytotoxicity results, electrical characterization, and computational outputs (DFT and NBO analyses), are available within the published article and its Supplementary Information. Additional raw data and scripts used for theoretical calculations have been deposited in Zenodo at https://zenodo.org/records/19135390. Further information can be requested from the corresponding author.

Ethics statement

Antimicrobial assays were performed using *Escherichia coli* JM109 (Gram-negative, biosafety level 1) following ASTM E2315-16 guidelines. Cytotoxicity tests were conducted on the human epithelial cell line MCF-7 (HTB-22, adenocarcinoma), purchased from ATCC and confirmed mycoplasma-free, in accordance with ISO 10993-5 standards. No experiments involved animals or human participants; therefore, ethical approval was not required.

Funding declaration

Thanks are due to (i) Made in Italy—Circular and Sustainable (MICS) Extended Partnership funded by the European Union Next-Generation EU (Piano Nazionale di Ripresa e Resilienza (PNRR)—Missione 4,

Componente 2, Investimento 1.3—D.D. 1551.11-10-2022, PE00000004); (ii) The Circular Economy Lab for Life Sciences-CELLS within the MUSA – Multilayered Urban Sustainability Action – project, funded by the European Union –NextGenerationEU, under the National Recovery and Resilience Plan (NRRP) Mission 4 Component 2 Investment Line 1.5: Strenghtening of research structures and creation of R&D "innovation ecosystems," set of "territorial leaders in R&D"; (iii) This project has received funding from the European Union's Horizon Europe research and innovation program under grant agreement No. 101070167 (ECOTRON project); (iv) MadABio project – funded by European Union – Next Generation EU within the PRIN 2022 PNRR program (D.D.1409 – September 14, 2022 Ministero dell'Università e della Ricerca).

Declaration of competing interest

The authors declare the following financial interests/personal relationships which may be considered as potential competing interests: VINCENZINA BARBERA reports financial support was provided by European Union. MAURIZIO GALIMBERTI reports financial support was provided by European Union. VINCENZINA BARBERA has patent #EP4196484A1 pending to Politecnico di Milano. Maurizio Galimberti has patent #EP4196484A1 pending to Politecnico di Milano. Gabriele Candiani has patent #EP4196484A1 pending to Politecnico di Milano. If there are other authors, they declare that they have no known competing financial interests or personal relationships that could have appeared to influence the work reported in this paper.

Acknowledgements

The authors thank Dr. Luigi Brambilla for performing the Raman analyses.

Appendix A. Supplementary data

Supplementary data to this article can be found online at https://doi.org/10.1016/j.carbon.2026.121464.

References

[1] A. Bianco, H.-M. Cheng, T. Enoki, Y. Gogotsi, R.H. Hurt, N. Koratkar, et al., All in the graphene family – a recommended nomenclature for two-dimensional carbon materials, Carbon N Y 65 (2013) 1–6, https://doi.org/10.1016/j.carbon.2013.08.038.

[2] K. Gouda, S. Bhowmik, B. Das, A review on allotropes of carbon and natural filler-reinforced thermomechanical properties of upgraded epoxy hybrid composite, Rev. Adv. Mater. Sci. 60 (2021) 237–275, https://doi.org/10.1515/rams-2021-0024.

[3] G. Tang, Z.-G. Jiang, X. Li, H.-B. Zhang, A. Dasari, Z.-Z. Yu, Three dimensional graphene aerogels and their electrically conductive composites, Carbon N Y 77 (2014) 592–599, https://doi.org/10.1016/j.carbon.2014.05.063.

[4] K. Ruan, X. Shi, Y. Guo, J. Gu, Interfacial thermal resistance in thermally conductive polymer composites: a review, Compos. Commun. 22 (2020) 100518, https://doi.org/10.1016/j.coco.2020.100518.

[5] H.H. Lara, E.N. Garza-Treviño, L. Ixtepan-Turrent, D.K. Singh, Silver nanoparticles are broad-spectrum bactericidal and virucidal compounds, J. Nanobiotechnol. 9 (2011) 30, https://doi.org/10.1186/1477-3155-9-30.

[6] P. Bélteky, A. Rónavári, N. Igaz, B. Szerencsés, I.Y. Tóth, I. Pfeiffer, et al., Silver nanoparticles: aggregation behavior in biorelevant conditions and its impact on biological activity, Int. J. Nanomed. 14 (2019) 667–687, https://doi.org/10.2147/IJN.S185965.

[7] J. Jana, S.S. Gauri, M. Ganguly, S. Dey, T. Pal, Silver nanoparticle anchored carbon dots for improved sensing, catalytic and intriguing antimicrobial activity, Dalton Trans. 44 (2015) 20692–20707, https://doi.org/10.1039/C5DT03858H.

[8] H. Tashan, K. Khosravi-Darani, F. Yazdian, M. Omidi, M. Sheikhpour, M. Farahani, et al., Antibacterial properties of graphene based nanomaterials: an emphasis on molecular mechanisms, surface engineering and size of sheets, Mini-Reviews Org. Chem. 16 (2019) 159–172, https://doi.org/10.2174/1570193X15666180712120309.

[9] G. Khandelwal, R. Kumar, V. Kumar, Antimicrobial activities of graphene–polymer nanocomposites, in: Nanostructured Polymer Composites for Biomedical Applications, Elsevier, 2019, pp. 429–445, https://doi.org/10.1016/B978-0-12-816771-7.00022-3.

[10] K. Hossain, M. Rafatullah, S.Z. Abbas, A. Ahmad, N. Ismail, A.Y. Maruthi, Antimicrobial activity of graphene-based nanomaterials, in: Graphene-Based Nanotechnologies for Energy and Environment, Elsevier, 2019, pp. 293–314, https://doi.org/10.1016/B978-0-12-815811-1.00016-8.

[11] L.-Y. Qu, J.-L. Liu, Y.-Y. Liu, G.-Q. Zhang, Y.-J. Xu, P. Zhu, et al., Anchoring silver nanoparticles using catechol-derived resins: an efficient and versatile approach for producing durable antimicrobial fabrics, Prog. Org. Coating 176 (2023) 107397, https://doi.org/10.1016/j.porgcoat.2022.107397.

[12] N.F. Attia, A.M. Eid, M.A. Soliman, M. Nagy, Exfoliation and decoration of graphene sheets with silver nanoparticles and their antibacterial properties, J. Polym. Environ. 26 (2018) 1072–1077, https://doi.org/10.1007/s10924-017-1014-5.

[13] X.-Z. Tang, X. Li, Z. Cao, J. Yang, H. Wang, X. Pu, et al., Synthesis of graphene decorated with silver nanoparticles by simultaneous reduction of graphene oxide and silver ions with glucose, Carbon N Y 59 (2013) 93–99, https://doi.org/10.1016/j.carbon.2013.02.058.

[14] R. Caudillo, X. Gao, R. Escudero, M. José-Yacaman, J.B. Goodenough, Ferromagnetic behavior of carbon nanospheres encapsulating silver nanoparticles, Phys. Rev. B 74 (2006) 214418, https://doi.org/10.1103/PhysRevB.74.214418.

[15] Y. Yu, L. Yan, M. Yue, H. Xu, Femtosecond laser-assisted synthesis of silver nanoparticles and reduced graphene oxide hybrid for optical limiting, R. Soc. Open Sci. 5 (2018), https://doi.org/10.1098/rsos.171436.

[16] A.F. de Faria, D.S.T. Martinez, S.M.M. Meira, A.C.M. de Moraes, A. Brandelli, A.G. S. Filho, et al., Anti-adhesion and antibacterial activity of silver nanoparticles supported on graphene oxide sheets, Colloids Surf. B Biointerfaces 113 (2014) 115–124, https://doi.org/10.1016/j.colsurfb.2013.08.006.

[17] M. Moghayedi, E.K. Goharshadi, K. Ghazvini, H. Ahmadzadeh, L. Ranjbaran, R. Masoudi, et al., Kinetics and mechanism of antibacterial activity and cytotoxicity of Ag-RGO nanocomposite, Colloids Surf. B Biointerfaces 159 (2017) 366–374, https://doi.org/10.1016/j.colsurfb.2017.08.001.

[18] L.L. Dong, Y.C. Ding, W.T. Huo, W. Zhang, J.W. Lu, L.H. Jin, et al., A green and facile synthesis for rGO/Ag nanocomposites using one-step chemical co-reduction route at ambient temperature and combined first principles theoretical analyze, Ultrason. Sonochem. 53 (2019) 152–163, https://doi.org/10.1016/j.ultsonch.2019.01.002.

[19] L.M. Hoyos-Palacio, D.P. Cuesta Castro, I.C. Ortiz-Trujillo, L.E. Botero Palacio, B. J. Galeano Upegui, N.J. Escobar Mora, et al., Compounds of carbon nanotubes decorated with silver nanoparticles via in-situ by chemical vapor deposition (CVD), J. Mater. Res. Technol. 8 (2019) 5893–5898, https://doi.org/10.1016/j.jmrt.2019.09.062.

[20] E.H. Falcao, F. Wudl, Carbon allotropes: beyond graphite and diamond, J. Chem. Technol. Biotechnol. 82 (2007) 524–531, https://doi.org/10.1002/jctb.1693.

[21] M. Galimberti, V. Barbera, S. Guerra, L. Conzatti, C. Castiglioni, L. Brambilla, et al., Biobased Janus molecule for the facile preparation of water solutions of few layer graphene sheets, RSC Adv. 5 (2015) 81142–81152, https://doi.org/10.1039/C5RA11387C.

[22] S. Naddeo, D. Gentile, F. Margani, G. Prioglio, F. Magaletti, M. Galimberti, et al., Pyrrole compounds from the two-step one-pot conversion of 2,5-Dimethylfuran for elastomer composites with low dissipation of energy, Molecules 29 (2024) 861, https://doi.org/10.3390/molecules29040861.

[23] V. Barbera, G. Leonardi, A.M. Valerio, L. Rubino, S. Sun, A. Famulari, et al., Environmentally friendly and regioselective one-pot synthesis of imines and oxazolidines serinol derivatives and their use for rubber cross-linking, ACS Sustainable Chem. Eng. 8 (2020) 9356–9366, https://doi.org/10.1021/acssuschemeng.0c01603.

[24] V. Barbera, L. Brambilla, A. Milani, A. Palazzolo, C. Castiglioni, A. Vitale, et al., Domino reaction for the sustainable functionalization of few-layer graphene, Nanomaterials 9 (2018) 44, https://doi.org/10.3390/nano9010044.

[25] S. Galimberti, V. Barbera, G. Candiani, Adduct Comprising at Least a Metal Selected from Gold, Silver and Copper and an Adduct of a Carbon Allotrop and a Pyrrolic Compound, 2023. US20230295188A1.

[26] S. Black, J.R. Ferrell, Determination of carbonyl groups in pyrolysis bio-oils using potentiometric titration: review and comparison of methods, Energy Fuels (2016), https://doi.org/10.1021/acs.energyfuels.5b02511 acs.energyfuels.5b02511.

[27] J.J.P. Stewart, Optimization of parameters for semiempirical methods IV: extension of MNDO, AM1 and PM3 to more main group elements, J. Mol. Model. 10 (2004) 155–164, https://doi.org/10.1007/S00894-004-0183-Z.

[28] D. Gentile, G. Floresta, V. Patamia, A. Nicosia, P.G. Mineo, A. Rescifina, Cucurbit [7]uril as a catalytic nanoreactor for one-pot synthesis of isoxazolidines in water, Org. Biomol. Chem. 18 (2020) 1194–1203, https://doi.org/10.1039/C9OB02352F.

[29] Gaussian 09, Revision A.02 – ScienceOpen n.d. https://www.scienceopen.com/document?vid=6be7271f-f651-464b-aee6-ef20b0743b6b (accessed May 20, 2025).

[30] C. Unger, M. Petsovits, P.A. Lieberzeit, P.A. Lieberzeit, A.A. Al-Saadi, Computational study of SERS effects in some aliphatic and cyclic carboxylic acids with silver nanomaterials, J. Phys., Conf. Ser. 1564 (2020) 012008, https://doi.org/10.1088/1742-6596/1564/1/012008.

[31] M.D. Hanwell, D.E. Curtis, D.C. Lonie, T. Vandermeerschd, E. Zurek, G. R. Hutchison, Avogadro: an advanced semantic chemical editor, visualization, and analysis platform, J. Cheminf. 4 (2012) 1–17, https://doi.org/10.1186/1758-2946-4-17/FIGURES/14.

[32] W. Kong, H. Kum, S.-H. Bae, J. Shim, H. Kim, L. Kong, et al., Path towards graphene commercialization from lab to market, Nat. Nanotechnol. 14 (2019) 927–938, https://doi.org/10.1038/s41565-019-0555-2.

[33] P. Zalar, L. Rubino, F. Margani, G. Kirchner, D. Raiteri, M.S. Galimberti, et al., A Janus molecule for screen-printable conductive carbon ink for composites with superior stretchability, Adv. Eng. Mater. 25 (2023), https://doi.org/10.1002/adem.202300706.

[34] S.V. Gudkov, I.V. Baimler, O.V. Uvarov, V.V. Smirnova, M.Y. Volkov, A. A. Semenova, et al., Influence of the concentration of Fe and Cu nanoparticles on the dynamics of the size distribution of nanoparticles, Front. Phys. 8 (2020), https://doi.org/10.3389/fphy.2020.622551.

[35] C.B. Whitehead, S. Özkar, R.G. Finke, LaMer's 1950 model for particle formation of instantaneous nucleation and diffusion-controlled growth: a historical look at the model's origins, assumptions, equations, and underlying sulfur sol formation kinetics data, Chem. Mater. 31 (2019) 7116–7132, https://doi.org/10.1021/acs.chemmater.9b01273.

[36] Z.H. Sheng, L. Shao, J.J. Chen, W.J. Bao, F.B. Wang, X.H. Xia, Catalyst-free synthesis of nitrogen-doped graphene via thermal annealing graphite oxide with melamine and its excellent electrocatalysis, ACS Nano 5 (2011) 4350–4358, https://doi.org/10.1021/NN103584T/SUPPL_FILE/NN103584T_SI_001.PDF.

[37] A. Proctor, P.M.A. Sherwood, X-ray photoelectron spectroscopic studies of carbon fibre surfaces—Ii: the effect of electrochemical treatment, Carbon N Y 21 (1983) 53–59, https://doi.org/10.1016/0008-6223(83)90156-2.

[38] J.R. Pels, F. Kapteijn, J.A. Moulijn, Q. Zhu, K.M. Thomas, Evolution of nitrogen functionalities in carbonaceous materials during pyrolysis, Carbon N Y 33 (1995) 1641–1653, https://doi.org/10.1016/0008-6223(95)00154-6.

[39] L. Bokobza, J.-L. Bruneel, M. Couzi, Raman spectra of carbon-based materials (from graphite to carbon black) and of some silicone composites, C (Basel) 1 (2015) 77–94, https://doi.org/10.3390/c1010077.

[40] L.G. Cançado, K. Takai, T. Enoki, M. Endo, Y.A. Kim, H. Mizusaki, et al., General equation for the determination of the crystallite size La of nanographite by Raman spectroscopy, Appl. Phys. Lett. 88 (2006), https://doi.org/10.1063/1.2196057.

[41] D. Locatelli, V. Barbera, L. Brambilla, C. Castiglioni, A. Sironi, M. Galimberti, Tuning the solubility parameters of carbon nanotubes by means of their adducts with Janus Pyrrole compounds, Nanomaterials 10 (2020) 1176, https://doi.org/10.3390/nano10061176.

[42] V. Barbera, A. Bernardi, A. Palazzolo, A. Rosengart, L. Brambilla, M. Galimberti, Facile and sustainable functionalization of graphene layers with pyrrole compounds, Pure Appl. Chem. 90 (2018) 253–270, https://doi.org/10.1515/pac-2017-0708.

[43] C.B. Whitehead, S.O. Zkar, R.G. Finke, LaMer's 1950 model for particle formation of instantaneous nucleation and diffusion-controlled growth: a historical look at the model's origins, assumptions, equations, and underlying sulfur sol formation kinetics data, Chem. Mater. (2019), https://doi.org/10.1021/acs.chemmater.9b01273.

[44] S.V. Gudkov, I.V. Baimler, O.V. Uvarov, V.V. Smirnova, M.Y. Volkov, A. A. Semenova, et al., Influence of the concentration of Fe and Cu nanoparticles on the dynamics of the size distribution of nanoparticles, Front. Phys. 8 (2020) 622551, https://doi.org/10.3389/fphy.2020.622551.

[45] K.R. Paton, E. Varrla, C. Backes, R.J. Smith, U. Khan, A. O'Neill, et al., Scalable production of large quantities of defect-free few-layer graphene by shear exfoliation in liquids, Nat. Mater. 13 (2014) 624–630, https://doi.org/10.1038/nmat3944.

[46] Y. Hernandez, V. Nicolosi, M. Lotya, F.M. Blighe, Z. Sun, S. De, et al., High-yield production of graphene by liquid-phase exfoliation of graphite, Nat. Nanotechnol. 3 (2008) 563–568, https://doi.org/10.1038/nnano.2008.215.